5184 *Chem. Mater.* **2010,** *22,* 5184–5198
DOI:10.1021/cm101145d

CHEMISTRY OF MATERIALS
Article

Correlation of Oxygen Storage Capacity and Structural Distortion in Transition-Metal-, Noble-Metal-, and Rare-Earth-Ion-Substituted CeO_2 from First Principles Calculation

Asha Gupta,[†] U. V. Waghmare,[‡] and M. S. Hegde*,[§]

[†]*Materials Research Centre, and* [§]*Solid State and Structural Chemistry Unit, Indian Institute of Science, Bangalore 560012, India, and* [‡]*Theoretical Sciences Unit, Jawaharlal Nehru Centre for Advanced Scientific Research, Bangalore 560064, India*

Received April 23, 2010. Revised Manuscript Received August 6, 2010

Oxygen storage/release (OSC) capacity is an important feature common to all three-way catalysts to combat harmful exhaust emissions. To understand the mechanism of improved OSC for doped CeO_2, we undertook the structural investigation by X-ray diffraction (XRD), X-ray photoelectron spectroscopy (XPS), H_2-TPR (temperature-programmed hydrogen reduction) and density functional theoretical (DFT) calculations of transition-metal-, noble-metal-, and rare-earth (RE)-ion-substituted ceria. In this report, we present the relationship between the OSC and structural changes induced by the dopant ion in CeO_2. Transition metal and noble metal ion substitution in ceria greatly enhances the reducibility of $Ce_{1-x}M_xO_{2-\delta}$ (M = Mn, Fe, Co, Ni, Cu, Pd, Pt, Ru), whereas rare-earth-ion-substituted $Ce_{1-x}A_xO_{2-\delta}$ (A = La, Y) have very little effect in improving the OSC. Our simulated optimized structure shows deviation in cation−oxygen bond length from ideal bond length of 2.34 Å (for CeO_2). For example, our theoretical calculation for $Ce_{28}Mn_4O_{62}$ structure shows that Mn−O bonds are in 4 + 2 coordination with average bond lengths of 2.0 and 3.06 Å respectively. Although the four short Mn−O bond lengths spans the bond distance region of Mn_2O_3, the other two Mn−O bonds are moved to longer distances. The dopant transition and noble metal ions also affects Ce coordination shell and results in the formation of longer Ce−O bonds as well. Thus longer cation−oxygen bonds for both dopant and host ions results in enhanced synergistic reduction of the solid solution. With Pd ion substitution in $Ce_{1-x}M_xO_{2-\delta}$ (M = Mn Fe, Co, Ni, Cu) further enhancement in OSC is observed in H_2−TPR. This effect is reflected in our model calculations by the presence of still longer bonds compared to the model without Pd ion doping. The synergistic effect is therefore due to enhanced reducibility of both dopant and host ion induced due to structural distortion of fluorite lattice in presence of dopant ion. For RE ions (RE = Y, La), our calculations show very little deviation of bonds lengths from ideal fluorite structure. The absence of longer Y−O/La−O and Ce−O bonds make the structure much less susceptible to reduction.

1. Introduction

Oxygen storage materials have become important after the introduction of catalytic treatment of automotive exhaust in early 1970s.[1] Three-way catalysts that can eliminate CO, HCs (hydrocarbons), and NO_x simultaneously have been used to control exhaust emissions. To widen the operating window of the catalyst for the fluctuating air-to-fuel ratio at the automobile converter, there was a need to develop a catalyst that can store oxygen in the oxygen-rich region and release oxygen in the oxygen-lean region.[2,3] Gandhi et al. first coined the term "oxygen storing" property for base metal oxides.[4] Yao and Yao[5] showed for the first time the oxygen storage capacity for CeO_2 and cited it as a suitable oxygen storage component for the three-way catalysis. Mechanism of OSC is given as

$$CeO_2 + \delta CO \rightarrow CeO_{2-\delta} + \delta CO_2;\ CeO_{2-\delta} + \delta/2O_2 \rightarrow CeO_2$$

indicating high endurance of ceria toward fluctuating oxygen vacancies under oxygen excess and deficient conditions. Application of oxygen storage/release property of ceria for automobile exhaust catalytic treatment has led to the development of ceria-based catalyst, and first among them is ceria-zirconia solid solution.[2,6−9] It is now well-established

*Corresponding author. E-mail: mshegde@sscu.iisc.ernet.in.

(1) Taylor, K. C. *Catal. Rev.−Sci. Eng.* **1993**, *35*, 25.
(2) Kaspar, J.; Fornasiero, P.; Hickey, N. *Catal. Today* **2003**, *77*, 419.
(3) Ozawa, M.; Kimura, M.; Isogai, A. *J. Alloys Compd.* **1993**, *193*, 73.
(4) Gandhi, H. S.; Graham, G. W.; McCabe, R. W. *J. Catal.* **2003**, *216*, 433.
(5) Yao, H. C.; Yao, Y. F. Y. *J. Catal.* **1984**, *86*, 254.
(6) Fornasiero, P.; Balducci, G.; Kaspar, J.; Meriani, S.; di Monte, R.; Graziani, M. *Catal. Today* **1996**, *29*, 47.
(7) Rao, G. R.; Kašpar, J.; Meriani, S.; Di Monte, R.; Graziani, M. *Catal. Lett.* **1994**, *24*, 107–112.
(8) Sugiura, M. *Catal. Surv. Asia* **2003**, *7*, 77–87.
(9) Fornasiero, P.; Di Monte, R; Rao, G. R.; Kaspar, J.; Meriani, S.; Trovarelli, A.; Graziani, M. *J. Catal.* **1995**, *151*, 168–177.

Published on Web 08/27/2010
© 2010 American Chemical Society

that addition of zirconia (ZrO_2) to ceria to form a stable solid solution greatly enhances the reducibility of the Ce^{4+} ion in the bulk material.[10] Understanding the mechanism associated with improved OSC of ceria-based mixed solid solutions is of importance for rational designing of future new materials. Local structure analysis of $Ce_{1-x}Zr_xO_2$ solid solution by many groups reported that the creation of long and short Zr−O bonds in 8-fold coordinated fluorite structure is responsible for the improved OSC observed for the solid solution.[11−13] Substitution of Zr^{4+} ion in the Ce^{4+} site therefore increases the reducibility of Ce^{4+} in CeO_2, though ZrO_2 itself is not a reducible oxide. Incorporation of reducible ion, such as Ti^{4+} and Sn^{4+}, at the Ce site is known to enhance the OSC of $Ce_{1-x}Ti_xO_2$[14] and $Ce_{1-x}Sn_xO_2$,[15] respectively. Because of the reducible nature of the dopant ion, the Sn^{4+}/Sn^{2+} and Ti^{4+}/Ti^{3+} redox couples can also participate in redox reactions along with the Ce^{4+}/Ce^{3+} couple. Further, the local coordination around Sn^{4+} or Ti^{4+} ion is different from that of an ideal fluorite CeO_2 structure because of the smaller ionic radii (Shannon ionic radii, r = 0.81 Å for Sn^{4+} and 0.74 Å for Ti^{4+}) compared to Ce^{4+} ion (r = 0.97 Å), which leads to considerable distortion in the ceria lattice. The computer simulation of such mixed oxides is a well-established tool of investigation for gaining insight into many of the chemical and physical properties of these materials. We have previously used this technique to study CeO_2-ZrO_2,[16] CeO_2-TiO_2,[17] CeO_2-SnO_2,[18] and $CeO_2-Fe_2O_3$[19] solid solution and deduced that local structural distortion of the oxygen sublattice results in long and short Ce−O and Zr−O, Ti−O, Sn−O, and Fe−O bonds, and the weak longer bonds are responsible for higher reducibility of these solid solutions. In contrast to the other earlier works reported in the literature,[11−13] we observed that in addition to distortion of oxygen sublattice around the dopant ion, coordination around host Ce^{4+} ion is also affected. On the basis of our EXAFS and DFT analysis, we found that Ce coordination is distorted from ideal 8−fold coordination to 4 + 4 type coordination in these solid solutions. Isovalent dopant ions (Zr^{4+}, Ti^{4+}, Sn^{4+}) substitution for Ce^{4+} site in the fluorite lattice forms stoichiometric solid solution. Substitution of trivalent rare-earth (RE) ions, forming solid solutions with ceria maintaining a stable fluorite lattice at varying doping regime,[20] are accompanied with oxygen vacancies to maintain charge neutrality. Miki et al. has reported that La^{3+} substitution in ceria alone does not enhance the OSC, and presence of additional noble metal is required for the enhancement.[21] In another report, La^{3+}-doped ceria is shown to enhance the OSC of mixed-ceria solid solution.[22] Therefore, the effect of substituting RE ion in CeO_2 on its OSC is still ambiguous.

CeO_2 can also form solid solutions with aliovalent transition elements like Cr, Mn, Cu, Pb, and Ru at varying ranges of stability and composition.[23−30] Transition metal oxides are active in many redox reactions, and incorporated in ceria lattice acts as a potential three-way catalyst. Considerable progress has been made to understand the structure, stability, and catalytic reactions for these solid solutions, but the key factor behind the improved OSC is still unclear. In this context, we undertook comprehensive investigation of the local structural distortions of transition-metal-ion-, noble-metal-ion-, and rare-earth-ion-substituted ceria by employing first-principles density functional calculations complemented with experimental studies of XRD, XPS, and H_2-TPR. Bond lengths and bond valences were derived from the optimized structure obtained from theoretical calculations. Comprehensive analysis of the bond lengths and bond valences were carried out to correlate structural distortions and redox properties with oxygen storage capacity observed for these solid solutions. Bond valence sum (BVS) is an empirical quantity potentially used in coordination chemistry to determine the oxidations states of metal ions from the metal−ligand bond distances.[31] Ionic radius of the dopant ions as well as their redox behavior plays an important role in enhancing the OSC of the ceria solid solution. Here we show that transition metal ion substituted ceria greatly enhances the reducibility of bulk material. OSC achieved for transition metal ions and noble metal ions doped ceria is very high relative to $Ce_{0.9}Zr_{0.1}O_2$ and comparable to $Ce_{0.9}Ti_{0.1}O_2$ and $Ce_{0.9}Sn_{0.1}O_2$ reported in the literature. In contrast, RE ion substitution has little effect in improving the OSC of CeO_2.

2. Experimental Section

$Ce_{1-x}M_xO_{2-\delta}$ (x = 0.1 and M = Mn, Fe, Co, Ni, Cu, La, Y), $Ce_{1-y}N_yO_{2-\delta}$ (y = 0.02 and N = Pd, Pt), and $Ce_{0.88}M_{0.1}Pd_{0.02}O_{2-\delta}$

(10) Baidya, T.; Hegde, M. S.; Gopalakrishnan, J. *J. Phys. Chem. B* **2007**, *111*, 5149.
(11) Nagai, Y.; Yamamoto, T.; Tanaka, T.; Yoshida, S.; Nonaka, T.; Okamoto, T.; Suda, A.; Sugiura, M. *Catal. Today* **2002**, *74*, 225.
(12) Vlaic, G.; Fornasiero, P.; Geremia, S.; Kaspar, J.; Graziani, M. *J. Catal.* **1997**, *168*, 386.
(13) Lemaux, S.; Bensaddik, A.; van der Eerden, A. M. J.; Bitter, J. H.; Koningsberger, D. C. *J. Phys. Chem. B* **2001**, *105*, 4810.
(14) Baidya, T.; Gayen, A.; Hegde, M. S.; Ravishankar, N.; Dupont, L. *J. Phys. Chem. B* **2006**, *110*, 5262.
(15) Baidya, T.; Gupta, A.; Deshpandey, P. A.; Madras, G.; Hegde, M. S. *J. Phys. Chem. C* **2009**, *113*, 4059.
(16) Dutta, G.; Waghmare, U. V.; Baidya, T.; Hegde, M. S.; Priolkar, K.; Sarode, P. *Catal. Lett.* **2006**, *108*, 165.
(17) Dutta, G.; Waghmare, U. V.; Baidya, T.; Hegde, M. S.; Priolkar, K.; Sarode, P. *Chem. Mater.* **2006**, *18*, 3249.
(18) Gupta, A.; Hegde, M. S.; Priolkar, K. R.; Waghmare, U. V.; Sarode, P. R.; Emura, S. *Chem. Mater.* **2009**, *21*, 5836–5847.
(19) Gupta, A.; Kumar, A.; Waghmare, U. V.; Hegde, M. S. *Chem. Mater.* **2009**, *21*, 4880.
(20) McBride, J. R.; Hass, K. C.; Poindexter, B. D.; Weber, W. H. *J. Appl. Phys.* **1994**, *76*, 7.
(21) Miki, T.; Ogawa, T.; Haneda, M.; Kakuta, N.; Ueno, A.; Matsura, S.; Sato, M. *J. Phys. Chem.* **1990**, *94*, 6464.
(22) Reddy, B. M.; Katta, L.; Thrimurthulu, G. *Chem. Mater.* **2010**, *22*, 467.
(23) Singh, P.; Hegde, M. S. *Chem. Mater.* **2009**, *22*, 762.
(24) Singh, P.; Hegde, M. S.; Gopalakrishnan, J. *Chem. Mater.* **2008**, *20*, 7268.
(25) Luo, J.-Y.; Meng, M.; Yao, J.-S.; Li, X.-G.; Zha, Y.-Q.; Wang, X.; Zhang, T.-Y. *Appl. Catal., B* **2009**, *87*, 92.
(26) Imamura, S.; Shono, M.; Okamoto, N.; Hamada, A.; Ishida, S. *Appl. Catal., A* **1996**, *142*, 279.
(27) Beckers, J.; Rothenberg, G. *Dalton Trans.* **2008**, 6573.
(28) Bera, P.; Hegde, M. S.; Mitra, S.; Sampath, S. *Chem. Commun.* **2001**, 927.
(29) Zhang, Y.; Andersson, S.; Muhammed, M. *Appl. Catal., B* **1995**, *6*, 325.
(30) Singh, P.; Hegde, M. S. *Chem. Mater.* **2009**, *21*, 3337.
(31) Palenik, G. J. *Inorg. Chem.* **1997**, *36*, 122.

(M = Mn, Fe, Co, Ni, Cu) were prepared by the solution combustion method using ceric ammonium nitrate, $M-$nitrate, and urea as the fuel. For transition metal substitution, $M-$nitrate was employed in combustion synthesis, whereas for noble-metal-ion substitution, palladium chloride and tetraamine platinum(II) nitrate were used. All the compounds were procured from Sigma-Aldrich in their highest purity form. The precursors were dissolved in minimum volume of HNO_3 and 20 mL of water in a 300 mL crystallizing dish to form a clear solution. The dish was then kept in a preheated furnace at 320 °C. The combustion started after dehydration, and the product was obtained within 60 s. The solid products were heated at 600 °C for 36 h before any further analysis. A typical combustion reaction for the synthesis of $Ce_{0.9}Ni_{0.1}O_{2-\delta}$ is given below

$$0.9(NH_4)_2Ce(NO_3)_6 + 0.1Ni(NO_3)_2 + 3.77CH_4N_2O \rightarrow Ce_{0.9}Ni_{0.1}O_{1.9} + 3.77CO_2 + 7.47N_2 + 11.14H_2O$$

A higher percentage of substitution has been achieved in some cases.[25] The main purpose of this report is to undertake detailed examination and comparison of OSC of transition metal and RE element substitution synthesized under similar conditions. Therefore, we chose 10 atom % substitution in ceria, which can be easily made by solution combustion.

Characterizations of the solid products were carried out by XRD on a Philips X'Pert diffractometer at a scan rate of 0.12°/min with 0.02° step size in the 2θ range between 10° and 90°. Structures were refined by the Rietveld method on the CeO_2-fluorite model by means of Fullprof program.[32] X-ray photoelectron spectra were recorded on a Thermo Fisher Scientific Multilab 2000 (England) instrument with Al Kα radiation (1486.6 eV). The binding energies reported here are with reference to graphite at 284.5 eV having an accuracy of ±0.1 eV. Prior to XPS recording, oxide samples were ground with 30% by weight of graphite powder and made into thin pellets to avoid development of any charging on the nonconducting samples while XPS recording. Oxygen storage/release properties of solid catalyst were studied by hydrogen uptake measurements (temperature programmed hydrogen reduction, H_2-TPR) in a microreactor (30 cm length and 0.4 cm internal diameter) employing 5.49% H_2/Ar (certified calibration gases mixture obtained from Chemix Specialty Gases and Equipment, Bangalore, India) with 30 sccm flow rate and 10 °C/min linear heating rate up to 600 °C over 100 mg of oxide. Volume of hydrogen intake/consumption by the sample was calibrated against CuO standard using an online thermal conducting detector (TCD).

3. Computational Methods

In the present paper, we use the periodic supercell approach, which has become quite a popular method in modeling defects. We use plane wave self-consistent field (PWscf)[33] implementation of DFT with periodic boundary conditions to relax the internal structure. Our total energy calculations are based on local density approximation (LDA) to the exchange correlation energy of electrons. Interaction between valence electrons and ionic cores is treated using first-principles ultrasoft pseudopotentials[34] and a plane wave basis with an energy cut off of 30 Ry in the representation of the Kohn−Sham wave functions was employed. Semicore states of Ce and M (= Mn, Fe, Co, Ni, Cu, La, Y Pt, Pd, and Ru) are included in the valence and spin polarization is not considered in our calculation. The total energy was minimized with respect to lattice constant for CeO_2 fluorite structure, whereas for the other system, the lattice parameter was kept constant at the values obtained from Rietveld refined XRD results, and only the internal atomic positions were relaxed to minimize the total energy. For all calculations reported in this paper, we modeled a large $2 \times 2 \times 2$ supercell (96 sites), derived from the conventional unit cell, which contains 32 formula units of CeO_2. The integrals over the Brillouin zone were sampled on $4 \times 4 \times 4$ k-point Monkhorst-Pack.[35] For simulation of transition-metal-ion-doped CeO_2, four out of thirty-two Ce atoms were replaced by M atoms which correspond to 12.5 at % substitution (which is close to our experimental compostion of 10 at % substitution), and the oxygen vacancies were created near the dopant atom to maintain charge neutrality. For example, in the case of Mn-doped ceria, Mn is primarily present in the +3 oxidation state (as will be seen in the Results section); therefore, two oxygen vacancies were created. For substitution of smaller percentage of noble metal in CeO_2, one Ce site is replaced by noble metal (=Pd, Pt, Ru) corresponding to dopant concentration of ~3 at %, and an oxide vacancy is created near the dopant atom to compensate for the charge created by the lower-valence ion substitution.

The bond lengths determined from the optimized structures are used to estimate bond valence of oxygen following the bond valence method described by I. D. Brown and M. O'Keeffe.[36] Bond valence is defined as (a) $s_i = \exp[-(R_i - R_0)/B]$ and (b) $s_i = (R_i/R_0)^{-N}$, where R_i is the ith bond length, R_0 is the length of a bond of unit valence, and B and N are the fitted parameters obtained from refs 36 and 37. The atomic valence V is obtained by summing the bond valencies associated with a particular ion given by $V = \Sigma_i S_i$.

4. Results and Discussion

4.1. XRD. Powder X-ray patterns were Rietveld refined by simultaneously varying 18 parameters including the overall scale factor, background parameters, unit cell, half-width, shape, anisotropic, and thermal parameters, along with the oxygen occupancy. As will be seen in the following section, relative concentrations of metal ions in each compound was determined by XPS studies and it agreed within the experimental error of 4% of the composition taken in the preparation. Oxidation states of the metal ions were obtained from XPS. The oxygen stoichiometry obtained from Rietveld refinement is in close agreement to the stoichiometry calculated taking the oxidation states of metal ions from XPS analysis within an error of 3−5%. Composition and the lattice parameters, R_{Bragg}, R_f, and χ^2 for all the compounds are listed in Table 1. The refined profiles (see Figure 1) indicate that the XRD pattern could be indexed to the fluorite structure with space group *Fm3m* and no characteristic transition/noble metal oxide peaks were observed in the diffractogram. We observe a small decrease in lattice parameter with Mn substitution in agreement with lower

(32) Rodriguez-Carvajal, J. *Multi-pattern Rietveld Refinement program Fullprof. 2k*, version 3.30; Laboratoire Léon Brillouin, CEA Saclay: Gif-sur-Yvette, France, June 2005.
(33) Baroni, S.; Dal Corso, A.; de Gironcoli, S.; Giannozzi, P. http://www.pwscf.org.
(34) Vanderbilt, D. *Phys. Rev. B* **1990**, *41*, 7892.
(35) Monkhorst, J. H.; Pack, J. D. *Phys. Rev. B* **1976**, *13*, 5188.
(36) Brown, I. D.; *Structure and Bonding in Crystals*; O'Keeffe, M., Navrotsky, A., Eds.; Academic Press: New York, 1981.
(37) Brese, N. E.; O'Keeffee, M. *Acta Crystallogr., Sect. B* **1991**, *47*, 192.

ionic radius (r) of the dopant ions (r for Mn^{3+} = 0.58 Å) compared to the host ion (Ce^{4+} = 0.97 Å). For Fe^{3+} (r = 0.55 Å) substitution, we expect a decrease in lattice parameter with Fe^{3+} substitution in CeO_2. But instead, we observe an increase in lattice parameter (see Table 1) for $Ce_{0.9}Fe_{0.1}O_{2-\delta}$ system. This is attributed to the presence of higher proportion of Ce^{3+} component in the solid solution.[19] Substitution of lower valence ion increases the concentration of oxide ion vacancies to maintain charge neutrality. Presence of oxide ion vacancies therefore will lead to an increase in lattice parameter. These counteractive interactions between smaller ionic radius of dopant ions and higher proportion of oxide ion vacancies will lead to only small change in lattice parameter. However, with Pd (r = 0.86 Å) ion substitution decrease in the lattice parameter is observed in all cases. Increase in lattice parameter for La^{3+} ion substitution in CeO_2 is in accordance with higher ionic radius for La^{3+} (r = 1.16 Å). Change in lattice parameter of the solid solutions in comparison to CeO_2 and absence of characteristic oxide peaks in the diffractogram confirms the formation of homogeneous solid solutions with the dopant ions incorporated in the ceria lattice.

Table 1. Rietveld Refined Lattice Parameters of As-Prepared Compounds

compd	lattice param (Å)	R_f	R_{Bragg}	χ^2
CeO_2	5.411[a]			
$Ce_{0.9}Mn_{0.1}O_{1.95}$	5.4108(3)	1.15	1.36	1.56
$Ce_{0.88}Mn_{0.1}Pd_{0.02}O_{1.93}$	5.4097(2)	1.35	1.65	1.12
$Ce_{0.9}Fe_{0.1}O_{1.88}$	5.4159(5)	1.78	1.71	2.34
$Ce_{0.88}Fe_{0.1}Pd_{0.02}O_{1.86}$	5.4124(8)	0.78	1.89	1.63
$Ce_{0.9}Co_{0.1}O_{1.95}$	5.4096(6)	1.42	1.24	1.80
$Ce_{0.88}Co_{0.1}Pd_{0.02}O_{1.93}$	5.4091(5)	1.18	1.14	1.87
$Ce_{0.9}Ni_{0.1}O_{1.90}$	5.4143(7)	0.73	1.33	0.96
$Ce_{0.88}Ni_{0.1}Pd_{0.02}O_{1.88}$	5.4137(7)	0.96	1.02	0.98
$Ce_{0.9}Cu_{0.1}O_{1.90}$	5.4101(2)	0.97	1.23	1.24
$Ce_{0.88}Cu_{0.1}Pd_{0.02}O_{1.88}$	5.4094(4)	0.92	1.93	1.31
$Ce_{0.9}La_{0.1}O_{1.95}$	5.4108(6)	1.43	1.28	0.94
$Ce_{0.9}Y_{0.1}O_{1.95}$	5.4244(4)	1.85	2.11	1.77
$Ce_{0.98}Pt_{0.02}O_{1.98}$	5.4102(2)	1.45	1.74	2.02
$Ce_{0.98}Pd_{0.02}O_{1.98}$	5.4103(4)	1.17	1.42	0.98

[a] JCPDS Card No. 340394.

4.2. XPS. To examine the active redox couples involved in the oxygen storage/release property of the ceria-based solid solution and the chemical states of the dopant and the host ions, we recorded XPS for the as-prepared and the reduced samples. The doped ceria oxides were subjected to temperature programmed reduction in hydrogen to a maximum temperature of 600 °C. For the purpose of recording XPS, the samples were mixed with 30 wt % graphite and made into a thin pellet. It was then subjected to reduction in hydrogen at 600 °C in a sealed tube. The reduced sample was then cooled to room temperature under hydrogen atmosphere, and then immediately transferred to preparative chamber of the spectrometer.

Careful analysis of Mn (2p) core level XP spectra (see Figure 2a) reveals that the spectrum obtained for the as-prepared sample is similar to those observed for α-Mn_2O_3 reported in the literature.[38] The binding energy peaks for $2p_{3/2}$ and $2p_{1/2}$ are at 642 and 653.6 eV and a satellite peak

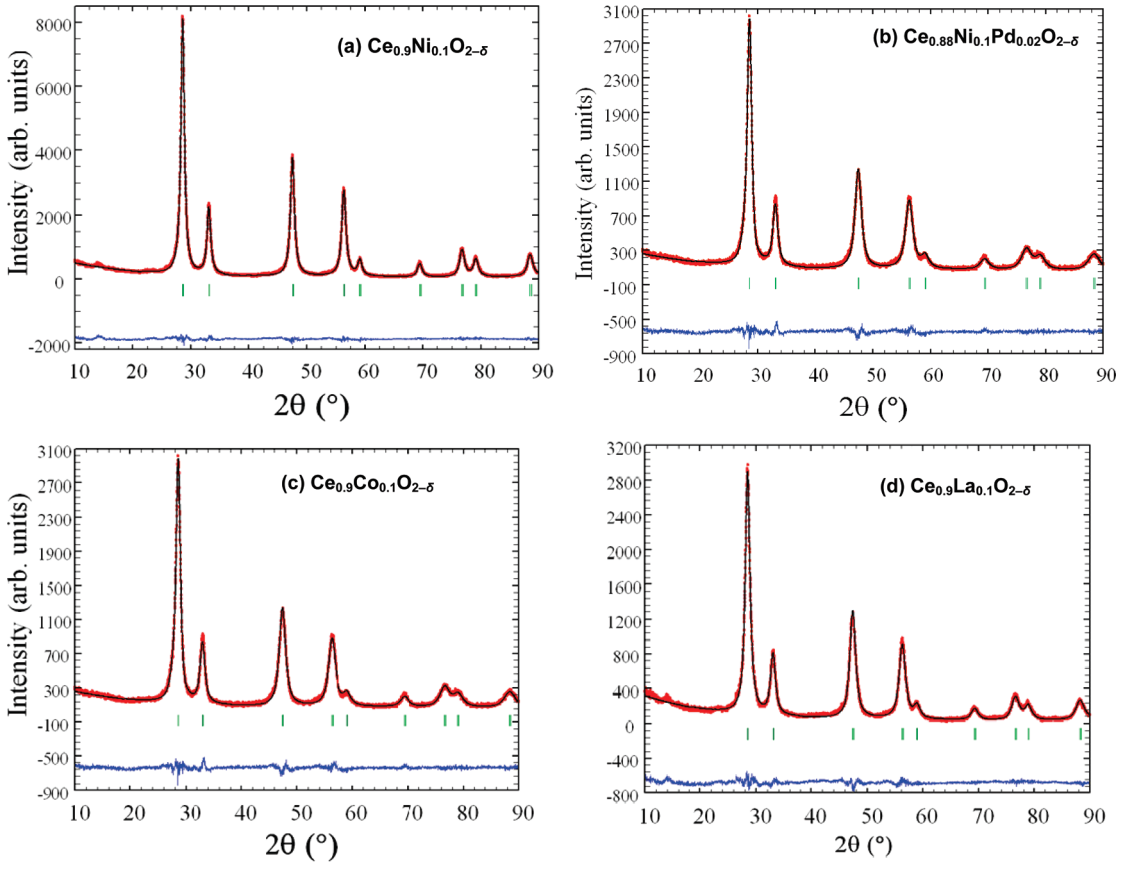

Figure 1. Rietveld refined XRD patterns of (a) $Ce_{0.9}Ni_{0.1}O_{2-\delta}$, (b) $Ce_{0.88}Ni_{0.1}Pd_{0.02}O_{2-\delta}$, (c) $Ce_{0.9}Co_{0.1}O_{2-\delta}$, and (d) $Ce_{0.9}La_{0.1}O_{2-\delta}$.

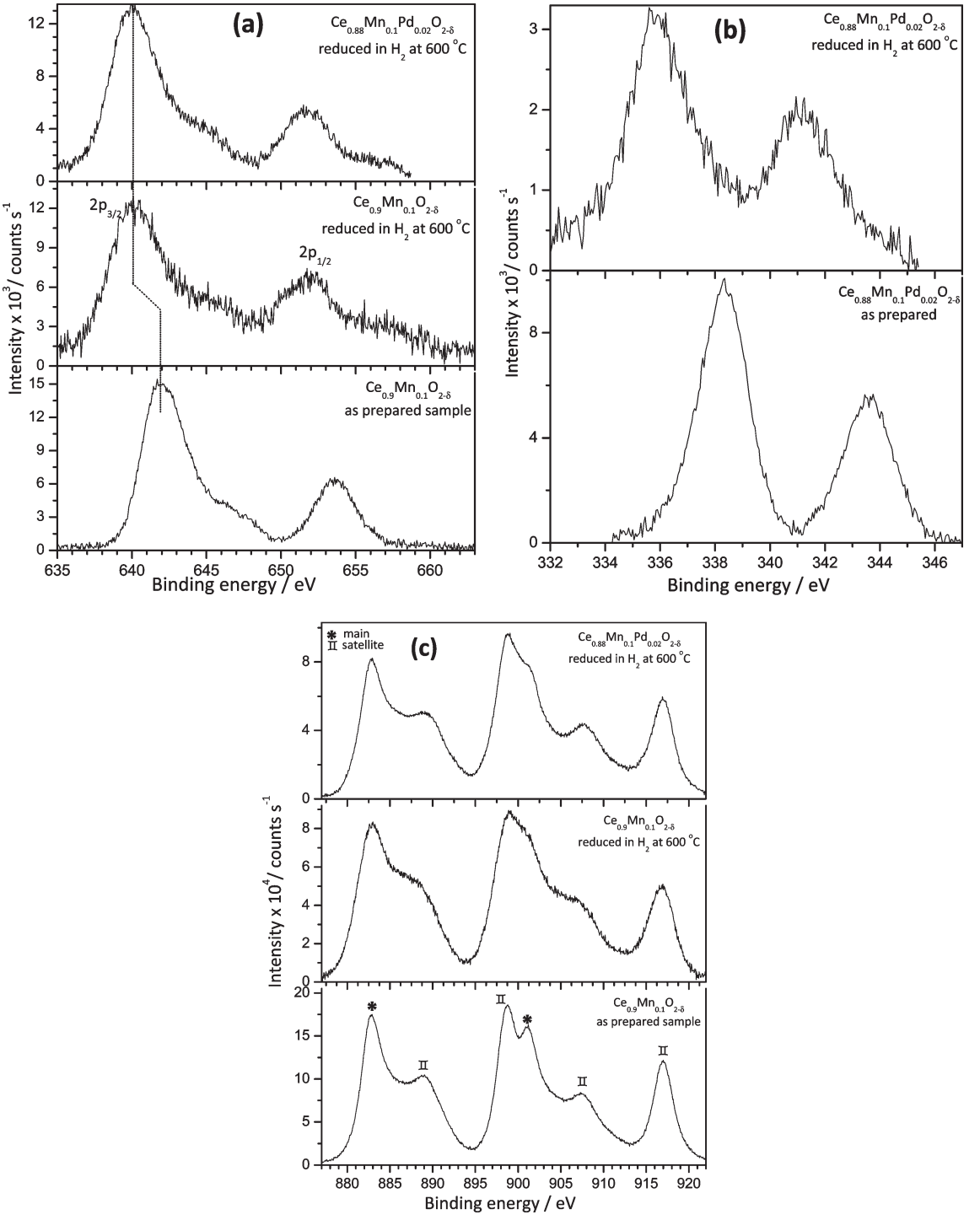

Figure 2. XPS regions of (a) Mn(2p), (b) Pd(3d), and (c) Ce(3d) of as-prepared and reduced samples of $Ce_{0.9}Mn_{0.1}O_{2-\delta}$ and $Ce_{0.88}Mn_{0.1}Pd_{0.02}O_{2-\delta}$.

~5 eV from the main peak. Mn (2p) core level spectra of the reduced sample is similar to those of MnO.[38] Therefore Mn is in +3 oxidation state in the as-prepared sample and in +2 oxidation state in the reduced sample. Similar Mn (2p) spectra are observed for as-prepared and reduced samples of $Ce_{0.88}Mn_{0.1}Pd_{0.02}O_{2-\delta}$. Binding energy of Pd ($3d_{5/2}$) is observed at 338.2 eV (Figure 2b) indicating that Pd is present in Pd^{2+} state in as prepared compound. The signal from Pd of the reduced sample appears at 335.1 eV indicating that Pd is reduced to lower oxidation state. The binding energy of metallic Pd appears at 335.1 eV,[39] while binding energy peak for Pd^{1+} appears at value higher than 335.1 eV.[40] For reduced $Ce_{0.88}Mn_{0.1}Pd_{0.02}O_2$ we observed signal in the Pd region at 335.1 eV, which indicates that Pd is primarily present in metallic state,

(38) Oku, M.; Hirokawa, K.; Ikeda, S. *J. Electron Spectrosc. Relat. Phenom.* **1975**, *7*, 465.

(39) Briggs, D.; Seah, M. P. *Practical Surface Analysis by Auger and X-Ray Photoelectron Spectroscopy*; John Wiley & Sons: New York, 1984; p 502.

(40) Shen, W.-J.; Ichihashi, Y.; Okumura, M.; Matsumura, Y. *Catal. Lett.* **2000**, *64*, 23.

though the possibility of Pd in +1 oxidation state due to incomplete reduction cannot be completely ruled out.

XPS of Ce (3d) core level (see Figure 2c) shows that Ce is mostly in +4 oxidation state with binding energy peaks at 883 and 901 eV corresponding to $3d_{5/2}$ and $3d_{3/2}$ core levels along with the characteristics satellite peaks due to Ce^{4+} state as in CeO_2.[41] Filling of the valley between the main and the satellite peak clearly indicate an increase in +3 component of Ce in the sample reduced in hydrogen. For the Pd-substituted sample, increment in Ce^{3+} concentration for the reduced sample is less compared to $Ce_{0.9}Mn_{0.1}O_{2-\delta}$.

Relative concentrations of the substituted dopant ions and Ce ion were determined from their core level intensities in each case. An estimation of relative concentration of Ce and Mn of as prepared and reduced catalyst were carried out from the intensities of main core level peaks[42]

$$\text{concentration, } C_M = \frac{\frac{I_M}{\lambda_M \sigma_M D_M}}{\sum\left(\frac{I_M}{\lambda_M \sigma_M D_M}\right)}$$

where I_M is the integrated intensity of the core levels (M = Ce 3d, Mn 2p), λ_M is the mean escape depths of the respective photoelectrons, σ_M is the photoionization cross section, and D_M is the geometric factor. The photoionization cross section values were taken from Scofield[43] and mean escape depths were taken from Penn.[44] The geometric factor was taken as 1, because the maximum intensity in this spectrometer is obtained at 90°. Accordingly, the relative surface concentrations of Ce:Mn:Pd obtained for as-prepared and spent samples were found to be same at 0.87:0.11:0.02, which is close to our experimental ratio. Therefore, no surface segregation of dopant ions after reduction cycle is observed.

Co ($2p_{3/2,1/2}$) core level spectra of the as-prepared $Ce_{0.9}Co_{0.1}O_{2-\delta}$ oxide appears at binding energy 780.3 and 795.4 eV respectively (see Figure 3a). The weak satellite peak observed in this case is signature of +3 oxidation state of Co.[45] Core level spectra in the Co (2p) region of the reduced sample have binding energy at 781.2 and 796.9 eV. A satellite peak at ~5 eV from $2p_{3/2}$ is similar to that observed for CoO in the literature.[45] Therefore in the as-prepared solid solution of $Ce_{0.9}Co_{0.1}O_{2-\delta}$, Co is predominantly present in +3 oxidation state whereas when treated with hydrogen at 600 °C reduction to +2 oxidation state occurs. Pd (3d) peak shows characteristic of +2 oxidation state in the as-prepared sample (Figure 3b). The Pd signal from the reduced sample shows very much broadening indicating the presence of metallic Pd in the reduced sample. Ce(3d) signals for the as-prepared sample shows that Ce is predominantly present in +4 state while upon reduction small change in the Ce signal indicate an increase in +3 oxidation state (Figure 3c). Relative concentrations of Ce:Co:Pd were estimated to be 0.90:0.08:0.02 for the as-prepared sample and 0.91:0.07:0.02 for the reduced sample which is close to each other, indicating no surface segregation after subjecting the sample to high-temperature reduction.

Ni (2p) in the as-prepared samples of $Ce_{0.9}Ni_{0.1}O_{2-\delta}$ and $Ce_{0.88}Ni_{0.1}Pd_{0.02}O_{2-\delta}$ appears at 854.5 and 872.5 eV and a strong satellite peak appears at ~6 eV from the main $2p_{3/2}$ line (Figure 4a). There is a difference of 18.2 eV between main $2p_{3/2}$ and $2p_{1/2}$ signals. These are the characteristics of Ni in +2 oxidation state.[46] For $Ce_{0.9}Ni_{0.1}O_{2-\delta}$ and $Ce_{0.88}Ni_{0.1}Pd_{0.02}O_{2-\delta}$ oxides reduced in H_2−TPR experiment, the signal from Ni ($2p_{3/2}$) is present at 852.2 eV, and the difference of 17.3 eV between the main peaks are characteristic of metallic Ni. Also we observe an increase of the shakeup peak at 857.8 eV, and the shakeup peak at 861.0 eV for Ni^{2+} has diminished in intensity for the reduced sample. Similar observations were made by Lambers et al.,[47] which indicates that Ni is primarily present in metallic state in the reduced sample. But the broad line shape suggests the presence of Ni in +2 oxidation state also along with the reduced metallic state. Binding energy peaks for Pd (3d) in the as-prepared oxide shows Pd in +2 oxidation state, and signal from the reduced oxide show the presence of both +2 and metallic Pd (Figure 4b). Ce (3d) peak presents characteristic signal for Ce in +4 oxidation state. For the reduced oxides we find an increase in +3 component of Ce as seen by the filling of valley between the main and satellite peaks. For Pd doped oxide the component of +3 oxidation state of Ce is higher. The relative ratio for the concentration of Ce:Ni:Pd estimated from the XPS signals are 0.87:0.11:0.02 for both as-prepared sample and reduced samples signifying no surface segregation of the dopant ions occurred after the oxidation−reduction cycle at higher temperatures.

The doublet signal from Cu (2p) core level in the as-prepared sample appears at 934 and 953.7 eV and a satellite to the main peak at 942.3 eV is assigned to Cu in +2 oxidation state (see the Supporting Information, Figure S1).[48] The signal from the reduced $Ce_{0.9}Cu_{0.1}O_{2-\delta}$ oxide show subsequent decrease in the satellite intensity indicating presence of mixed valence state of Cu. A shift from 934 to 932.5 eV is observed for signal from Cu ($2p_{3/2}$) of reduced $Ce_{0.88}Cu_{0.1}Pd_{0.02}O_{2-\delta}$ oxide; the satellite intensity further decreases. Signal for Pd (3d) shows a shift from +2 to 0 oxidation state in the reduced sample. We also observe an increase in Ce^{3+} component in the reduced oxides compared to the as-prepared oxide.

XPS spectra corresponding to Y (3d) region acquired from $Ce_{0.9}Y_{0.1}O_{2-\delta}$ oxide shows doublet due to splitting into $3d_{5/2}$ and $3d_{3/2}$ states (see Figure S2 in the Supporting Information). The binding energy peaks for $3d_{5/2}$ appears

(41) Kotani, A.; Ogasawara, H. *J. Electron Spectrosc. Relat. Phenom.* **1992**, *60*, 257.
(42) Powell, C. J.; Larson, P. E. *Appl. Surf. Sci.* **1978**, *1*, 186.
(43) Scofield, J. H. *J. Electron Spectrosc. Relat. Phenom.* **1976**, *8*, 129.
(44) Penn, D. R. *J. Electron Spectrosc. Relat. Phenom.* **1976**, *9*, 29.
(45) Jiménez, V. M.; Espinós, J. P.; González-Elipe, A. R. *Surf. Interface Anal.* **1998**, *26*, 62.
(46) Grosvenor, A. P.; Biesinger, M. C.; Smart, R. S. C.; McIntyre, N. S. *Surf. Sci.* **2006**, *600*, 1771.
(47) Lambers, E. S.; Dykstal, C. N.; Seo, J. M.; Rowe., J. E.; Holloway, P. H. *Oxid. Met.* **1996**, *45*, 301.
(48) Ghodselahi, T.; Vesaghi, M. A.; Shafiekhani, A.; Baghizadeh, A.; Lameii, M. *Appl. Surf. Sci.* **2008**, *255*, 5.

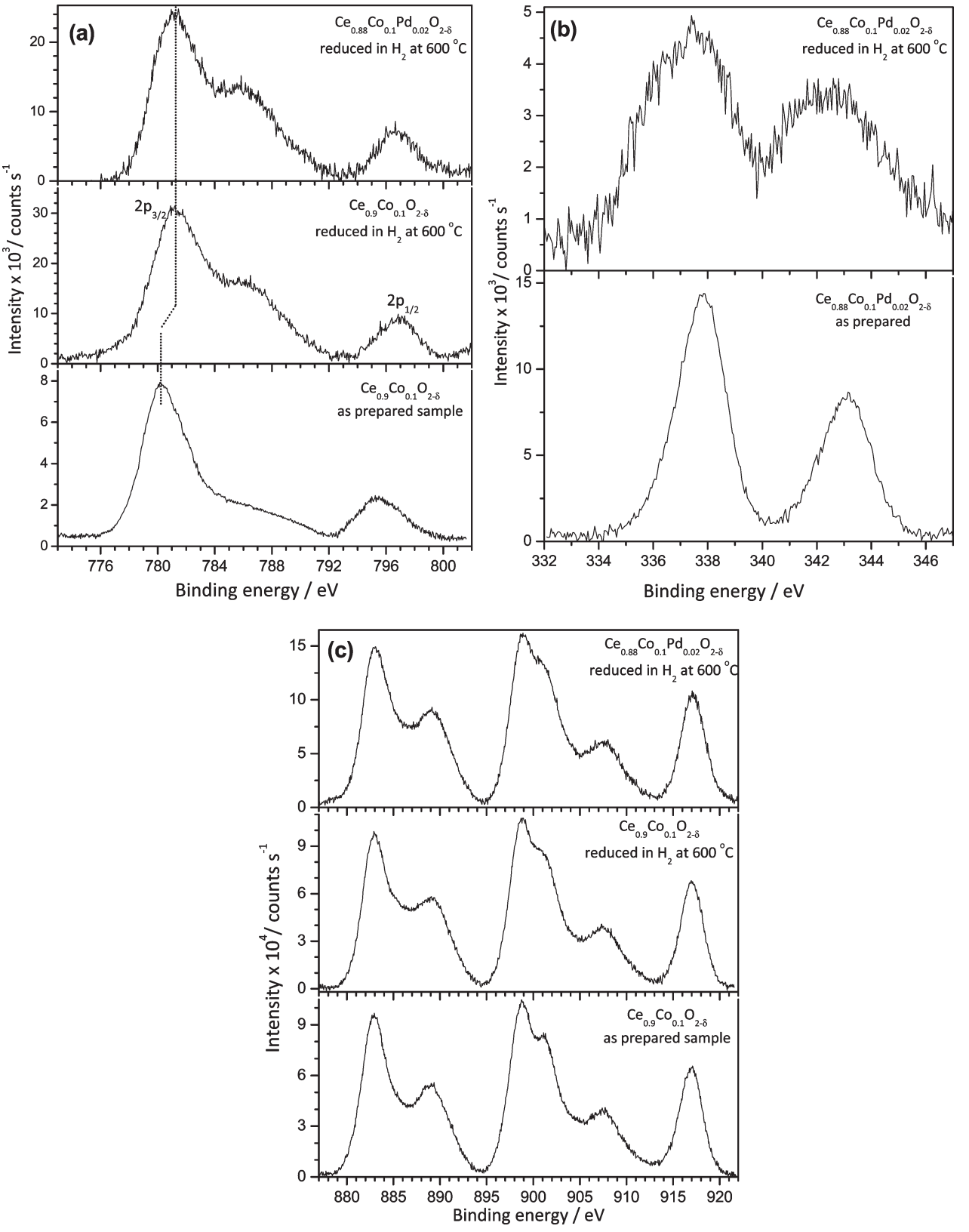

Figure 3. XPS regions of (a) Co(2p), (b) Pd(3d), and (c) Ce(3d) of as-prepared and reduced samples of $Ce_{0.9}Co_{0.1}O_{2-\delta}$ and $Ce_{0.88}Co_{0.1}Pd_{0.02}O_{2-\delta}$.

at 158 eV which corresponds to +3 oxidation state.[49] The signal from the reduced oxide shows similar profile indicating unreduced state of Y^{3+}. Signal from Ce (3d) region of the as-prepared oxide shows Ce in +4 oxidation state. Filling of valley between the main and satellite peak shows increase in +3 component of Ce in the reduced oxide. Therefore $Ce_{0.9}Y_{0.1}O_{2-\delta}$ sample subjected to reduction

(49) Yu Kirikova, N.; Krupa, J. C.; Makhov, V. N.; Severac, C. *J. Electron Spectrosc. Relat. Phenom.* **2002**, *122*, 5.

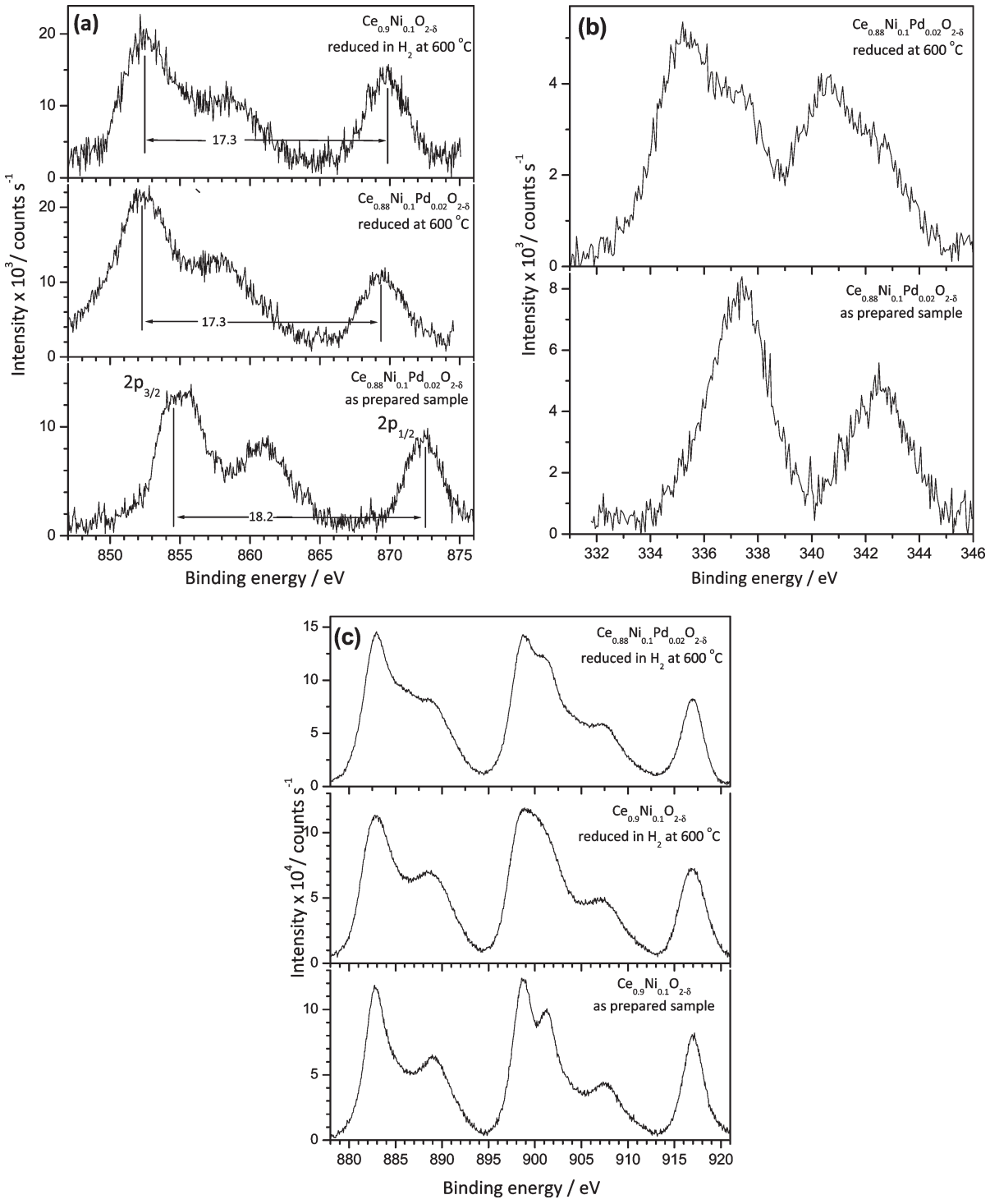

Figure 4. XPS regions of (a) Ni(2p), (b) Pd(3d), and (c) Ce(3d) of as-prepared and reduced samples of $Ce_{0.9}Ni_{0.1}O_{2-\delta}$ and $Ce_{0.88}Ni_{0.1}Pd_{0.02}O_{2-\delta}$.

shows hydrogen consumption corresponding to Ce^{4+} reduction only, and Y^{3+} remains unaltered. A similar result is obtained for $Ce_{0.9}La_{0.1}O_{2-\delta}$ oxide. No shift in binding energy position for the La ($3d_{5/2}$, $_{3/2}$) peak at 835 and 851.7 eV is observed for the reduced oxide (see Figure S3), indicating that La is in the +3 oxidation state in both the as-prepared and reduced compound.[50] However, a noticeable change in Ce spectra for the reduced sample indicates an increase in +3 oxidation state for the reduced oxide. Therefore, in La-doped ceria, any reduction observed corresponds to Ce^{4+} to Ce^{3+} reduction, and no contribution comes from La reduction.

4.3. H_2−TPR. Temperature-programmed hydrogen reduction techniques have been extensively used to measure the OSC of the mixed ceria solid solution. To derive the effect of substituting transition metal ions and rare-earth ions in ceria lattice on its oxygen storage/release

(50) Bogdanchikova, N. E.; Fuentes, S.; Avalos-Borja, M.; Farías, M. H.; Boronin, A.; Díaz, G. *Appl. Catal., B* **1998**, *17*, 221.

Table 2. OSC and Composition of As-Prepared Samples and after Reduction in H_2−TPR at 600 °C

composition		
as prepared	reduced	OSC (μmol of [O]/g of catalyst)[a]
CeO_2	$CeO_{1.96}$	230
$Ce^{4+}_{0.9}Mn^{3+}_{0.1}O_{1.95}$	$Ce^{4+}_{0.74}Ce^{3+}_{0.16}Mn^{2+}_{0.1}O_{1.82}$	800
$Ce^{4+}_{0.88}Mn^{3+}_{0.1}Pd^{2+}_{0.02}O_{1.93}$	$Ce^{4+}_{0.68}Ce^{3+}_{0.30}Mn^{2+}_{0.1}Pd^{0}_{0.02}O_{1.71}$	1350
$Ce^{4+}_{0.76}Ce^{3+}_{0.14}Fe^{3+}_{0.1}O_{1.88}$	$Ce^{4+}_{0.64}Ce^{3+}_{0.26}Fe^{2+}_{0.1}O_{1.77}$	675
$Ce^{4+}_{0.74}Ce^{4+}_{0.14}Fe^{3+}_{0.1}Pd^{2+}_{0.02}O_{1.86}$	$Ce^{4+}_{0.56}Ce^{3+}_{0.32}Fe^{2+}_{0.1}Pd^{0}_{0.02}O_{1.70}$	955
$Ce^{4+}_{0.9}Co^{3+}_{0.1}O_{1.95}$	$Ce^{4+}_{0.84}Ce^{3+}_{0.06}Co^{2+}_{0.1}O_{1.87}$	510
$Ce^{4+}_{0.88}Co^{3+}_{0.1}Pd^{2+}_{0.02}O_{1.93}$	$Ce^{4+}_{0.68}Ce^{3+}_{0.2}Co^{2+}_{0.1}Pd^{0}_{0.02}O_{1.76}$	1050
$Ce^{4+}_{0.9}Ni^{2+}_{0.1}O_{1.90}$	$Ce^{4+}_{0.88}Ce^{3+}_{0.02}Ni^{0}_{0.1}O_{1.79}$	670
$Ce^{4+}_{0.88}Ni^{2+}_{0.1}Pd^{2+}_{0.02}O_{1.88}$	$Ce^{4+}_{0.86}Ce^{3+}_{0.02}Ni^{0}_{0.1}Pd^{0}_{0.02}O_{1.75}$	750
$Ce^{4+}_{0.9}Cu^{2+}_{0.1}O_{1.90}$	$Ce^{4+}_{0.82}Ce^{3+}_{0.08}Cu^{0}_{0.1}O_{1.76}$	855
$Ce^{4+}_{0.88}Cu^{2+}_{0.1}Pd^{2+}_{0.02}O_{1.88}$	$Ce^{4+}_{0.70}Ce^{3+}_{0.18}Co^{0}_{0.1}Pd^{0}_{0.02}O_{1.67}$	1250
$Ce^{4+}_{0.9}La^{3+}_{0.1}O_{1.95}$	$Ce^{4+}_{0.82}Ce^{3+}_{0.08}La^{3+}_{0.1}O_{1.91}$	245
$Ce^{4+}_{0.9}Y^{3+}_{0.1}O_{1.95}$	$Ce^{4+}_{0.80}Ce^{3+}_{0.10}Y^{3+}_{0.1}O_{1.90}$	350
$Ce^{4+}_{0.98}Pt^{2+}_{0.01}O_{1.98}$	$Ce^{4+}_{0.93}Ce^{3+}_{0.05}Pt^{0}_{0.01}O_{1.935}$	255
$Ce^{4+}_{0.9}Pd^{2+}_{0.1}O_{1.98}$	$Ce^{4+}_{0.94}Ce^{3+}_{0.04}Pd^{2+}_{0.1}O_{1.94}$	232
$Ce^{4+}_{0.78}Ce^{3+}_{0.12}Ru^{4+}_{0.1}O_{1.94}$	$Ce^{4+}_{0.32}Ce^{3+}_{0.54}Ru^{0}_{0.1}O_{1.52}$	2512[30]

[a] OSC values given here in for hydrogen reduction up to 600 °C.

property, we carried out detailed analysis of H_2−TPR experiments. The values of OSC and composition of the reduced compound are summarized in Table 2.

For 10 at % Mn-substituted CeO_2, hydrogen uptake starts at ∼100 °C and peaks at 245 °C (T_{max}, highest intensity peak) (see Figure.5a). The reduction continues at higher temperature up to 600 °C, with two small reduction peaks appearing at ∼400 and 500 °C. The OSC measured from hydrogen reduction up to 600 °C for $Ce_{0.9}Mn_{0.1}O_{2-\delta}$ solid solution is 800 μmol [O]/g compared to 230 μmol [O]/g of pure CeO_2. To assess the change in reduction behavior of Mn ion in CeO_2 lattice in comparison to Mn_2O_3, we completed H_2−TPR of Mn_2O_3 (dotted line in Figure.5). Mn_2O_3 shows two reduction peaks at 375 and 470 °C. The total integrated area under the curve corresponds to reduction of $Mn_2O_3 + H_2 \rightarrow 2MnO + H_2O$. The ratio of the first (∼375 °C) to second (∼470 °C) reduction peaks is 2. The first reduction peak is ascribed to reduction of Mn_2O_3 to Mn_3O_4 and the second peak is generated because of reduction of Mn_3O_4 to MnO.[51] Combined result of H_2−TPR and XPS show that reduction of Mn^{3+} in $Ce_{0.9}Mn_{0.1}O_{2-\delta}$ is shifted to lower temperature compared to reduction of Mn_2O_3. This implies that Mn^{3+} ion in CeO_2 lattice is more reducible compared to Mn_2O_3. Reduction of Ce^{4+} to Ce^{3+} in the mixed oxide is also shifted to lower temperature compared to reduction of CeO_2.[14] These observations provide the presence of synergistic interaction in the mixed ceria lattice which enhances the reducibility of both Mn and Ce ions. For $Ce_{1-x}Zr_xO_2$ system, substitution of Zr enhances the reducibility of Ce ion only and Zr^{4+} remains nonreducible. But in Mn substituted CeO_2, reducibility of both the host and the dopant ions are improved. With the substitution of Pd ion in $Ce_{0.9}Mn_{0.1}O_{2-\delta}$ striking change in the reduction behavior is observed. The reduction which was occurring at elevated temperature in absence of Pd ion is now shifted to 130 °C. OSC for Pd doped system is also higher (1350 μmol/g; see Table 2) indicating improved reducibility of $Ce_{0.88}Mn_{0.1}Pd_{0.02}O_{2-\delta}$ compound. TPR results show that synergistic interaction between Pd, Mn, and Ce ions has a more intense effect in terms of (a) enhancement of OSC and (b) decreasing the temperature at which enhanced OSC is accomplished.

H_2−TPR profiles for α-Fe_2O_3 in comparison to $Ce_{0.9}Fe_{0.1}O_{2-\delta}$ oxides are shown in Figure S4. Two-stage reduction is observed for α-Fe_2O_3 −the first reduction peak at ∼390 °C arises due to reduction of Fe_2O_3 to Fe_3O_4 followed by further reduction to metallic Fe at higher temperature.[52] H_2−TPR profiles of $Ce_{0.9}Fe_{0.1}O_{2-\delta}$ exhibits peak reduction ∼400 °C and continues until 600 °C. Estimate of composition of the reduced oxide from the H_2−TPR combined with XPS data reveals that reduction of Fe^{3+} to Fe^{2+} and partial reduction of Ce^{4+} to Ce^{3+} occurs at 600 °C. Synergistic interaction between Fe and Ce ion bring down the temperature for reduction of Fe^{3+} to Fe^{2+} in comparison to reduction of Fe_2O_3 to Fe. Also Fe^{3+} ion in $Ce_{0.9}Fe_{0.1}O_{2-\delta}$ is reduced only up to +2 oxidation state (derived from XPS results) and presence of metallic Fe is not observed even for reduction at 600 °C. Similar to Mn doped ceria, we observe that with the addition of Pd ion in $Ce_{0.9}Fe_{0.1}O_{2-\delta}$ higher reducibility is achieved at comparatively lower temperatures.

Reduction of Co_3O_4 (see Figure.5b) takes place in two stages −first stage corresponds to reduction of $Co_3O_4 + H_2 \rightarrow 3CoO + H_2O$ appears as a shoulder around 350 °C and second reduction at ∼400 °C corresponds to reduction of $3CoO + 3H_2 \rightarrow Co + 3H_2O$.[53] $Ce_{0.9}Co_{0.1}O_{2-\delta}$ shows many low temperature reduction peak and the highest intensity peak is centered at ∼400 °C. XPS analysis show reduction of Co^{3+} to metallic Co does not occur for $Ce_{0.9}Co_{0.1}O_{2-\delta}$ compound subjected to reduction up to 600 °C. Synergistic interaction between Ce and Co in the mixed solid solution gives rise to low temperature reduction. With Pd ion substitution we see an enormous increase in OSC and the reduction occurs at a much lower temperature of 150 °C. Therefore, for Co-doped CeO_2, the presence of Pd ion induces additional synergistic effect between the cations, leading to an increase in OSC and decrease in reduction temperature.

Reduction of NiO is observed as a single step broad reduction centered at ∼370 °C (Figure.5c). The integrated area under the curve corresponds to reduction of NiO to metallic Ni.[54] The broad reduction peak for $Ce_{0.9}Ni_{0.1}O_{2-\delta}$ solid solution is centered at ∼300 °C and no further reduction is observed after ∼350 °C. Unlike the previous transition metal ions, Ni^{2+} reduces to metallic state (as seen from XPS results). With the incorporation of Pd ion in the solid solution, a very sharp reduction is observed at ∼70 °C, and a second broad reduction peak appears starting from 200 to 400 °C. The high-temperature

(51) Lin, R.; Liu, W.-P.; Zhong, Y.-J.; Luo, M.-F. *React. Kinet. Catal. Lett.* **2001**, *72*, 289.
(52) Galvita, V.; Sundmacher, K. *J. Mater. Sci.* **2007**, *42*, 8.
(53) Bulavchenko, O. A.; Cherepanova, S. V.; Malakhov, V. V.; Dovlitova, L. S.; Ishchenko, A. V.; Tsybulya, S. V. *Kinet. Catal.* **2009**, *50*, 7.
(54) Yuexiang, Z.; Guiping, X.; Youchang, X. *Acta Phys. Chim. Sin.* **1999**, *15*, 91.

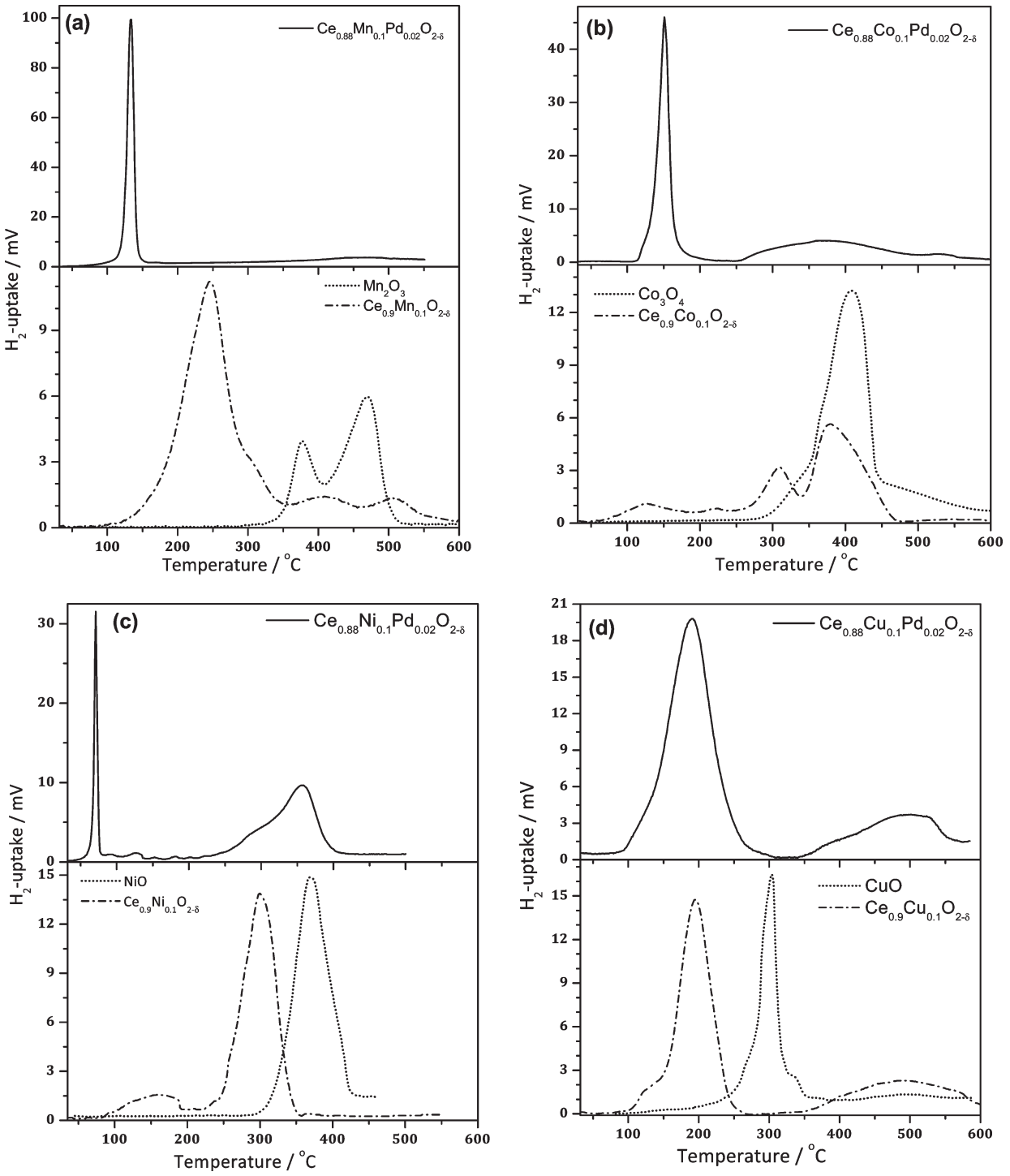

Figure 5. H_2−TPR profiles of (a) Mn_2O_3, $Ce_{0.9}Mn_{0.1}O_{2-\delta}$ and $Ce_{0.88}Mn_{0.1}Pd_{0.02}O_{2-\delta}$, (b) Co_3O_4, $Ce_{0.9}Co_{0.1}O_{2-\delta}$ and $Ce_{0.88}Co_{0.1}Pd_{0.02}O_{2-\delta}$, (c) NiO, $Ce_{0.9}Ni_{0.1}O_{2-\delta}$ and $Ce_{0.88}Ni_{0.1}Pd_{0.02}O_{2-\delta}$, and (d) CuO, $Ce_{0.9}Cu_{0.1}O_{2-\delta}$ and $Ce_{0.88}Cu_{0.1}Pd_{0.02}O_{2-\delta}$.

peak is shifted toward the higher side compared to sample without Pd ion. The area corresponding to the sharp low-temperature peak for $Ce_{0.88}Ni_{0.1}Pd_{0.02}O_{2-\delta}$ is rather small and contribution to the overall OSC of 790 μmol/g comes from the high temperature peak, indicating less-pronounced synergistic effect due to Pd-ion substitution.

Reduction of CuO starts from 150 °C and peaks at 300 °C (see Figure 5d). The integrated area under the curve corresponds to reduction of CuO to Cu.[55] For $Ce_{0.9}Cu_{0.1}O_{2-\delta}$ oxide the broad reduction signal is centered at 195 °C, followed by high-temperature reduction from 350 °C onward. Cu^{2+} reduces to its metallic state upon reduction (as observed from XPS analysis). Synergistic interaction between Ce and Cu ions results in decreased temperature of reduction for these ions. For $Ce_{0.88}Cu_{0.1}Pd_{0.02}O_{2-\delta}$ solid solution, we observe very little decrease in peak reduction temperature from 195 to 190 °C followed by a second broad

(55) Priolkar, K. R.; Bera, P.; Sarode, P. R.; Hegde, M. S.; Emura, S.; Kumashiro, R.; Lalla, N. P. *Chem. Mater.* **2002**, *14*, 2120–2128.

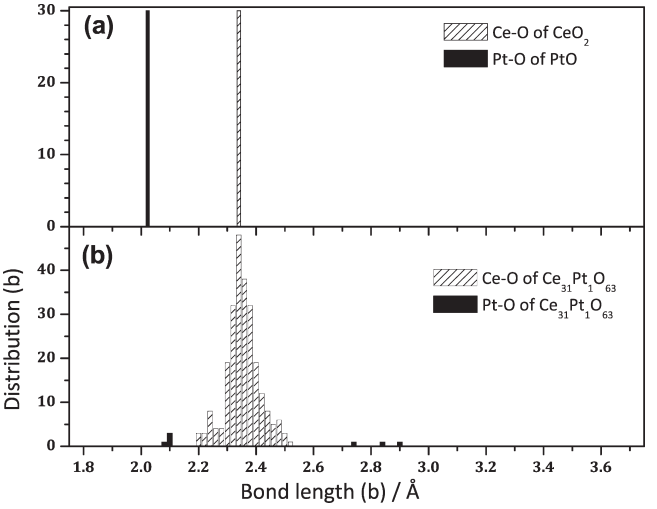

Figure 6. Distribution of M—O (M = Pt, Ce) bond lengths of (a) PtO and CeO_2 and (b) $Ce_{31}Pt_1O_{63}$.

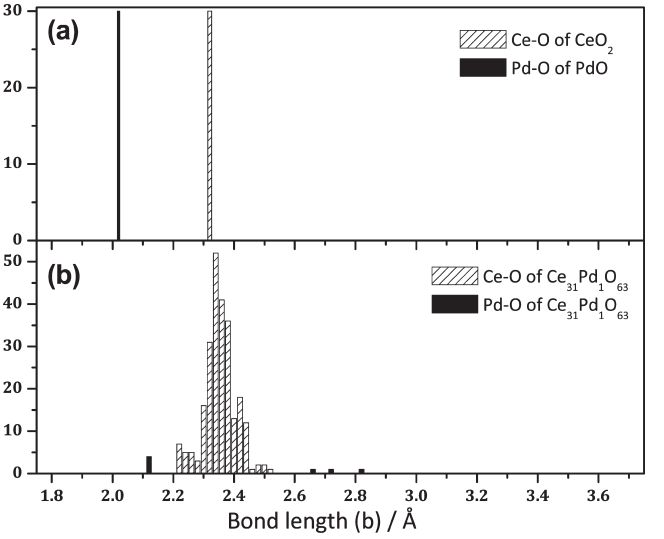

Figure 7. Distribution of M—O (M = Pd, Ce) bond lengths of (a) PdO and CeO_2 and (b) $Ce_{31}Pd_1O_{63}$.

reduction peak at higher temperatures. The synergistic effect brought about by Pd-ion substitution has very little effect in lowering the temperature of reduction, but resulted in overall increase in OSC for Pd substituted $Ce_{0.9}Cu_{0.1}O_{2-\delta}$ solid solution.

To summarize our results for H_2−TPR in conjunction with XPS, we have seen that Mn^{3+} in ceria lattice reduces only to Mn^{2+} oxidation state. Similarly, Fe^{3+} and Co^{3+} ion in $Ce_{0.9}Fe_{0.1}O_{2-\delta}$ and $Ce_{0.9}Co_{0.1}O_{2-\delta}$ respectively reduces only up to Fe^{2+} and Co^{2+} oxidation state and further reduction to their metallic state is not observed when treated with hydrogen at 600 °C. Whereas for Ni and Cu doped ceria the dopant ions reduces to their metallic state. Because of the metallic nature of the reduced state of the dopant ions, it is more likely to undergo phase separation via sintering when subjected to higher temperature reduction for longer duration. The effect of sintering will be absent for Mn-, Fe-, and Co-doped ceria, which remains in ionic state after reduction. It is worth noting that for Mn-, Fe-, and Co-doped ceria, the higher OSC is achieved at lower temperatures on adding Pd ion in the solid solution. Such effect on adding Pd ion in $Ce_{0.9}Ni_{0.1}O_{2-\delta}$ and $Ce_{0.9}Cu_{0.1}O_{2-\delta}$ solid solution is less pronounced. Therefore, Ni- and Cu-doped ceria are inferior choices for OSC compared to Mn-, Fe-, and Co-doped ions.

H_2-uptake studies for rare-earth-element-substituted $Ce_{0.9}Y_{0.1}O_{2-\delta}$ and $Ce_{0.9}La_{0.1}O_{2-\delta}$ systems show very little increment in OSC compared to the effect caused by transition metal ion substitution (see Figure S5 in the Supporting Information; note the y-scale). Small increase (see Table 2) in OSC is only due to Ce^{4+} to Ce^{3+} reduction, and the dopant RE ion does not participate in the redox mechanism. OSC for 10 at % transition-metal-ion-substituted ceria is comparable to $Ce_{1-x}Zr_xO_2$,[56] $Ce_{1-x}Ti_xO_2$,[14] and $Ce_{1-x}Sn_xO_2$,[15] and 10 at % Ru is reported to show very high OSC.[30]

(56) Fally, F.; Perrichon, V.; Vidal, H.; Kaspar, J.; Blanco, G.; Pintado, J. M.; Bernal, S.; Colon, G.; Daturi, M.; Lavalley, J. C. *Catal. Today* **2000**, *59*, 373–386.

In an attempt to understand the underlying phenomenon of improved OSC, we performed local structural investigation and bond valence analysis by simulating the ceria-based structures theoretically based on first-principles density functional theory.

4.4. DFT. Our calculated undoped CeO_2 bulk supercell has an optimized lattice constant of 5.42 Å, which is close to the experimental value of 5.411 Å (JCPDS No. 340394), with all Ce−O bond lengths equal to 2.34 Å (see Figure 6). Both PtO and PdO crystallize in tetragonal symmetry with the noble metal in square-planar geometry. All four Pt−O and Pd−O bond lengths are equal to 2.023 and 2.018 Å, respectively (shown in Figures 6 and 7). With Pt and Pd substitution, the simulated optimized structure $Ce_{32}Pt_1O_{63}$ and $Ce_{32}Pd_1O_{63}$ shows deviation in cation−oxygen bond length from ideal bond length of 2.34 Å (for CeO_2). Both Pt and Pd exhibit 4 + 3 coordination in the solid solution. The four short Pt−O bond lengths are ~2.1 Å and the three long Pt−O bond length distributed over region of 2.75−2.9 Å. For Pd-doped structure, all four Pd−O bond lengths are equal at 2.12 Å, and the three long bonds exhibits similar distribution at longer distances between 2.66 and 2.82 Å. Distribution of Ce−O bonds reveals the local geometry around the cations is distorted from ideal structure. The deviation of Ce−O bond length is small and mostly centered around the ideal bond length of 2.34 Å. This indicates the presence of strain in the lattice due to dopant ion substitution leading to changes in the bond lengths.

Bond valence sum (BVS) gives an idea about the oxidation states of the metal ions in these simulated structures which can be further extended to explore the underlying chemical behavior of the doped ions. BVS for the cations and oxide ions were estimated from the optimized bond lengths. BVS for Pt in $Ce_{32}Pt_1O_{63}$ is 1.83 and for Ce is 3.99, indicating that Pt ion is underbonded, leading to easy reducibility compared to Ce ion. Few oxide ions for $Ce_{32}Pt_1O_{63}$ structure are found to have BVS as low as 1.55, whereas few others exhibit BVS of

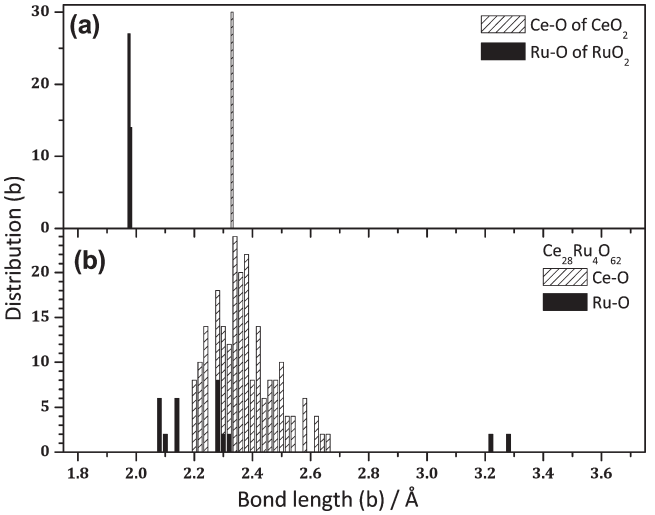

Figure 8. Distribution of M—O (M = Ru, Ce) bond lengths of (a) RuO_2 and CeO_2, (b) $Ce_{28}Ru_4O_{62}$.

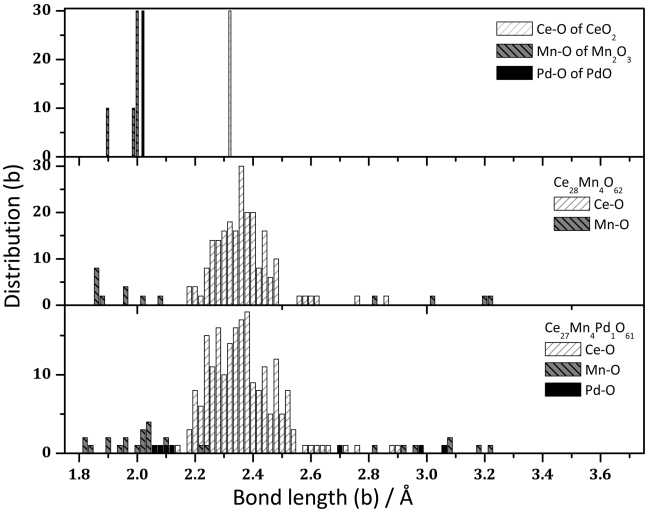

Figure 9. Distribution of M—O (M = Pd, Mn, Ce) bond lengths of Mn_2O_3, PdO, CeO_2, $Ce_{28}Mn_4O_{62}$,and $Ce_{27}Mn_4Pd_1O_{61}$.

~2.3. Similar assessment of BVS for Pd and Ce in $Ce_{32}Pd_1O_{63}$ is 1.92 and 3.99 indicating higher reducibility of Pd compared to Ce. In this case, oxide ions with BVS of 1.45 are detected compensated by increased BVS of 2.3 by others oxide ions. The oxide ions with relatively low BVS are chemically more reactive toward reduction. Thus the synergistic effect in the doped ceria solid solution is attributed to local structural distortion induced by the dopant ions leading to creation of strain in the lattice. This is followed by changes in the cation−oxygen bond lengths and subsequent changes in bond valences. The oxide ions with lower bond valences are relatively loosely held in the lattice by surrounding cations, and are therefore responsible for higher OSC. It is noted that oxide ions that form longer bonds with Ce have lower BVS. Removal of these oxide ions will induce reduction of Ce^{4+} ion. Therefore, along with the Pd^{2+}/Pd^0 or $Pt^{4+}/Pt^{2+}/Pt^0$ redox couple, Ce^{4+}/Ce^{3+} redox reactions are also promoted. It is because of this reason higher H/Pt or H/Pd ratio phenomena have been observed for Pt/CeO_2 and Pd/CeO_2 systems.[57,58]

RuO_2 crystallizes in tetragonal geometry with space group $P4_2/mnm$. Ru is in rectangular pyramidal symmetry with the four planar Ru−O bonds equal to 1.975 Å and the two apical Ru−O bonds equal to 1.982 Å (shown in Figure 8). Ten atom % Ru is reported[30] to form solid solution with CeO_2 with very high OSC (see Table 2). For theoretical calculations, $Ce_{28}Ru_4O_{62}$ supercell was used to simulate the structure. Ru−O bonds are distributed over three regions in a 3:4:1 ratio. The average Ru−O bond lengths are 2.11, 2.28, and 3.23 Å. The Ce−O bonds are distributed over a region 2.2−2.7 Å. BVS estimated for Ru from the optimized bonds lengths is 2.21. This indicates that Ru^{4+} ion in the ceria lattice is highly reducible. The very high OSC reported for $Ce_{0.9}Ru_{0.1}O_{2-\delta}$ system is attributed to highly reducible Ru−O bonds, which in turn induces easy reduction of Ce^{4+}.

Mn_2O_3 crystallizes in the $Ia\bar{3}$ space group with Mn in two coordinating environments, (i) Mn is six coordination with all Mn−O bond lengths equal to 2.003 Å, and (ii) Mn in four coordination with 2 Mn−O bond lengths equal to 1.897 Å and the other two equal to 1.987 Å. These bonds lengths are represented in Figure9 along with the Pd−O and Ce−O bond length. The cation−oxygen bonds are extracted from the optimized structure of $Ce_{28}Mn_4O_{62}$ and the distribution is shown in Figure 9. It is easy to comprehend from the bond distribution that Mn−O bond distances show more deviation from ideal bond length of 2.34 Å compared to Ce−O bonds. Mn is in 4 + 2 coordination with the short Mn−O bond distances are confined within 1.8−2.1 Å while the long distances are above 2.8 Å. Therefore, the short Mn−O distance spans the bond distance region of Mn_2O_3, and the other Mn−O bonds are moved to longer distances. It may be noted that large changes in the Mn−O bond distances observed for the optimized structure cannot be only due Jahn−Teller distortion commonly known for Mn^{3+} ion. Jahn−Teller distortion for Mn ion will result in changes of bond lengths of about 1−2%,[59−61] whereas in the present case, we see huge changes (about 30%) in Mn−O bond length.

Unlike Mn−O bonds which show bunching at two different regions, Ce−O bonds are distributed over a continuous range of bond distances indicating deviation from normal eight−fold coordination. Note that some Ce−O bonds are unusually long. The synergistic interaction we observed for Mn doped CeO_2 in H_2−TPR experiments can now be related to structural changes induced by the dopant Mn ion. For Pd substituted $Ce_{27}Mn_4Pd_1O_{61}$ structure further increase in the bond lengths distribution is noticed (see the change in the

(57) Bera, P.; Gayen, A.; Hegde, M. S.; Lalla, N. P.; Spadaro, L.; Frusteri, F.; Arena, F. *J. Phys. Chem. B* **2003**, *107*, 10.
(58) Baidya, T.; Dutta, G.; Hegde, M. S.; Waghmare, U. V. *Dalton Trans.* **2009**, 455.
(59) Louca, D.; Kwei, G. H. *Phys. Rev. Lett.* **1998**, *80*, 3811.
(60) Wu, S. Y.; Hwang, S. R.; Li, W.-H.; Lee, K. C.; Lynn, J. W.; Liu, R. S. *Chin. J. Chem. Phys.* **2000**, *38*, 354.
(61) Mitchell, J. F.; Argyriou, D. N.; Potter, C. D.; Hinks, D. G.; Jorgensen, J. D.; Bader, S. D. *Phys. Rev. B* **1996**, *54*, 6172.

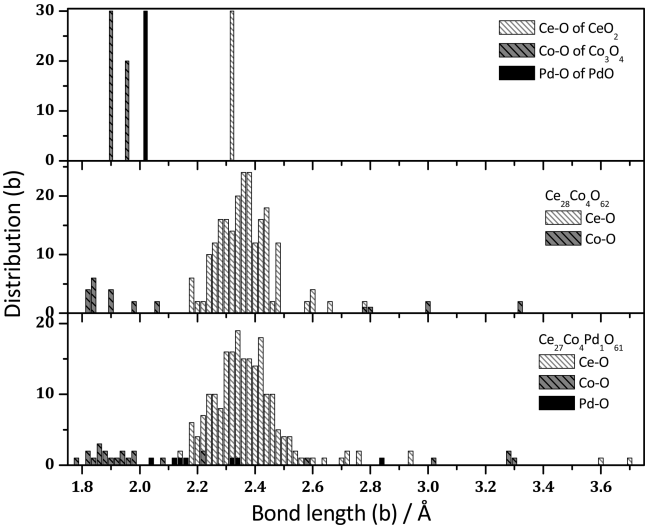

Figure 10. Distribution of M—O (M = Pd, Co, Ce) bond lengths of Co_3O_4, PdO, CeO_2, $Ce_{28}Co_4O_{62}$,and $Ce_{27}Co_4Pd_1O_{61}$.

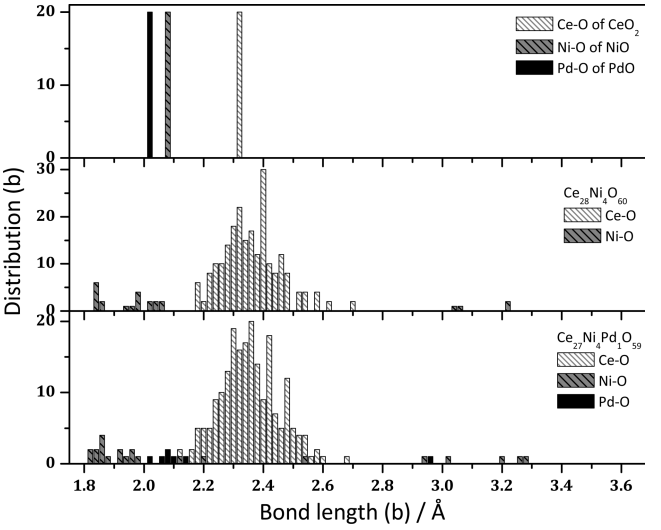

Figure 11. Distribution of M—O (M = Pd, Ni, Ce) bond lengths of NiO, PdO, CeO_2, $Ce_{28}Ni_4O_{60}$, and $Ce_{27}Mn_4Pd_1O_{59}$.

y-scale as well). High OSC in H_2-TPR is reflected in still longer Pd−O, Mn−O and Ce−O bonds (see Figure 9). BVS estimated for Mn is 3.08 in concordance with formal oxidation state of +3. BVS estimated for Ce ions are within 3.85−4.05 indicating the presence of both underbonded and overbonded Ce. Estimation of BVS for the oxide show values in the range 1.55−2.25 (see Figure S6 in the Supporting Information). With Pd ion substitution we find the variation in BVS has further increased (note the *y*-scale of Figure S6 in the Supporting Information), indicating higher reducibility.

We have previously studied Fe substituted ceria system and theoretical results for $Ce_{28}Fe_4O_{62}$ and $Ce_{27}Fe_4Pd_1O_{61}$ are given in details therein.[19] From DFT calculations, it is found that the oxygen sublattice is highly distorted in $Ce_{0.9}Fe_{0.1}O_{1.88}$ and $Ce_{0.89}Fe_{0.1}Pd_{0.01}O_{1.84}$ compared to CeO_2 and $Ce_{0.99}Pd_{0.1}O_{2-\delta}$, leading to formation of long and short M−O (M = Fe, Pd, Ce) bonds. The presence of longer oxygen bonds decreases the oxygen bond valence to approximately −1.5, leading to activation of lattice oxygen, which in turn is responsible for the high OSC property observed in the catalysts. On the basis of valence band analysis from XPS, it is proposed that synergistic electronic interaction between the valence states of Pd, Fe, and Ce ions are responsible for high OSC at lower temperatures for Pd- and Fe-doped ceria.

Fe ion in the simulated structure exhibits short and long Fe−O bonds. The longer Fe−O bonds indicate higher reducibility of the dopant ion. The presence of dopant ion results in longer Ce−O bonds also. Therefore, the synergistic reduction of both longer Ce−O and Fe−O bonds leads to higher OSC compared to only CeO_2. With Pd substitution, the optimized structure results in still longer bonds, which explains the higher OSC for Pd substituted solid solution.

Co_3O_4 crystallizing $F\bar{4}3m$ space group has two types of Co−O bond distances: (i) Co^{3+} in octahedral geometry with all 6 Co−O bond distances equal to 1.903 Å, and (ii) Co^{2+} in tetrahedral geometry with Co−O bond equal to 1.956 Å (see Figure 10). Co doping in ceria was simulated with $Ce_{28}Co_4O_{62}$ model creating oxide ion vacancy taking Co in +3 oxidation state (from our XPS results). Co−O bonds show bunching in short and long bond lengths region. The coordination shell around Co ion is 4 + 2 and their average bond lengths are 1.88 and 3.05 Å respectively. The four short Co−O distances spans the region of Co_3O_4 bonds lengths, and the other Co−O bonds are moved much longer distances. Ce−O bonds show continuous distribution around 2.34 Å with some Ce−O bonds present at unusually longer distances. Thus the dopant Co ion in CeO_2 leads to formation of longer Co−O and Ce−O bonds. With Pd doping we see an additional distribution in the bond lengths leading to enhanced reducibility. Co^{3+} ions are underbonded in $Ce_{28}Co_4O_{62}$ structure with BVS of 2.85 and 2.93, and BVS for Ce^{4+} ions are within 3.76−4.01. Estimation of bond valences for Co-doped structure show the presence of oxide ion with BVS of 1.4.

NiO crystallizes in $Fm\bar{3}m$ space group with Ni in octahedral coordination and Ni−O bond lengths equals to 2.089 Å (see Figure 11). $Ce_{0.9}Ni_{0.1}O_{2-\delta}$ was simulated using a structural model of $Ce_{28}Ni_4O_{60}$ considering Ni in +2 oxidation state. The ratio of the short and long bond distances and hence the coordination shell of Ni is found to be 5:1 from our simulations and the average of the short and long bond lengths are 1.93 and 3.13 Å respectively. Long Ce−O bond lengths (above 2.7 Å) as seen to be present in the previous cases (see Figure.9 and 10) are not found for Ni simulated structure. Absence of longer Ce−O bonds explain the behavior of decreased synergistic effect observed for $Ce_{0.9}Ni_{0.1}O_{2-\delta}$ in H_2−TPR experiment. For $Ce_{27}Ni_4Pd_1O_{59}$ structure, few longer Pd−O and Ce−O bonds are also detected, which is responsible for only a small increase in OSC for $Ce_{0.88}Ni_{0.1}Pd_{0.02}O_{2-\delta}$. Bond valence computed from the optimized structure show that Ni ion is slightly overbonded with BVS of 2.11.

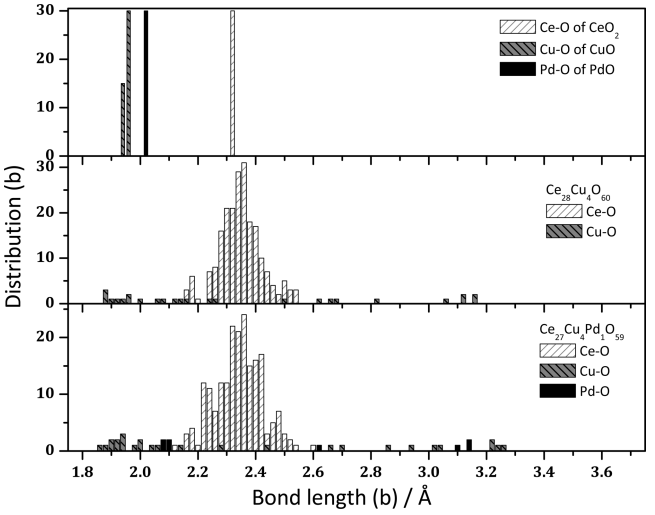

Figure 12. Distribution of M—O (M = Pd, Cu, Ce) bond lengths of CuO, PdO, CeO_2, $Ce_{28}Cu_4O_{60}$, and $Ce_{27}Cu_4Pd_1O_{59}$.

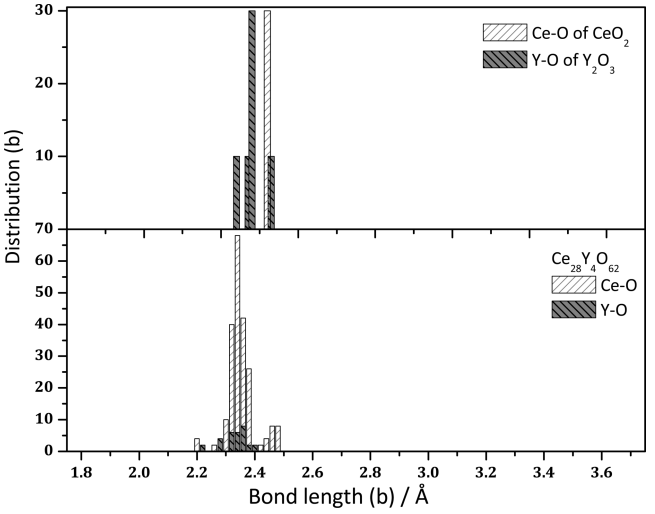

Figure 13. Distribution of M—O (M = Y, Ce) bond lengths of Y_2O_3, CeO_2, and $Ce_{28}Y_4O_{62}$.

CuO crystallizes in $C2/c$ space group (monoclinic) with two types of Cu−O bonds− 1.95 and 1.96 Å (see Figure 12). Cu doped ceria structure is simulated with $Ce_{28}Cu_4O_{60}$ supercell taking into consideration that Cu is +2 oxidation state (from XPS data). Cu−O bond are obtained in two distinct regions. Cu for our simulated structure shows 4 + 3 coordination with 2.01 and 2.83 Å−the average short and long bond lengths respectively. With Pd doping, Cu−O bonds further shifts to longer distance. Ce−O bonds longer than 2.7 Å are not obtained for Cu doped simulated sturtcures. Because of the absence of longer Ce−O bonds, the effect of synergism is less-pronounced for Cu- and Pd-doped ceria. BVS for Cu ion is calculated to be 1.8, indicating that Cu^{2+} ion in underbonded, whereas BVS for Ce ion is close to 3.95, showing slight underbonding character.

For $Ce_{28}Y_4O_{62}$ and $Ce_{28}La_4O_{62}$ structures, bond distance distributions show small deviation from the ideal bond distance of 2.34 Å (see Figures13 and 14). Both Ce−O and Y−O/La−O bonds are concentrated around the mean bond distance. For La doping, the shift toward

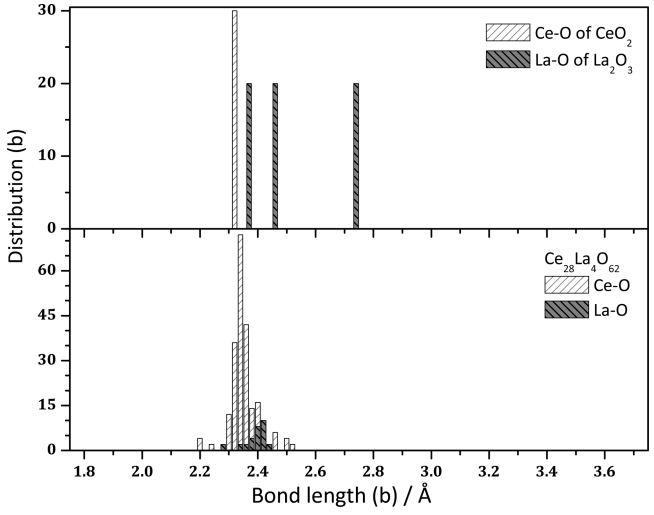

Figure 14. Distribution of M—O (M = La, Ce) bond lengths of La_2O_3, CeO_2, and $Ce_{28}La_4O_{62}$.

higher bond distance is in agreement with the higher ionic radius of La^{3+} ion relative to Ce^{4+}. The absence of longer Ce−O and La−O/Y−O bonds indicates very poor reducibility of the solid solution. BVS for the optimized structure reveals that both La and Y are overbonded with an average BVS of 3.37 and 4.44, respectively, and BVS for Ce is close to 4. This analysis indicates that dopant and host ions are not reducible in nature, imparting very small OSC capacity for their solid solutions in agreement with the H_2−TPR results.

5. Conclusions

Substitution of 10 at % transition metal greatly enhances the reducibility of $Ce_{0.9}M_{0.1}O_{2-\delta}$ (M = Mn, Fe, Co, Ni, Cu). OSC achieved for transition-metal-ion-doped ceria is very high relative to $Ce_{0.9}Zr_{0.1}O_2$ and comparable to $Ce_{0.9}Ti_{0.1}O_2$ and $Ce_{0.9}Sn_{0.1}O_2$. Therefore, these transition metal ions can be promising candidate as a dopant in ceria to enhance the OSC. On the contrary, RE ion substitution has very little effect in improving the OSC. XPS analysis show that dopant ions Mn, Fe, and Co are not reduced to their metallic state when subjected to reduction at higher temperature and they remain ionic in nature. On the contrary, Ni and Cu ions are reduced to their metallic state under hydrogen reduction cycles. Because of the metallic nature of the reduced state of Ni and Cu ions, it limits their application in catalysis because of problems arising from sintering of metallic Ni and Cu. We used DFT calculations to elucidate the relationship between improved OSC and structural modification due to doping. A direct correlation between the results of H_2-TPR and DFT calculations are observed. All the transition metal ions, namely Mn, Fe, Co, Ni, and Cu, and noble metal ions (Pd, Pt, and Ru) showed very high structural distortion. The structural distortion induced by dopant ions substitution generates long and short cation—oxygen bonds. Bond valence analysis for these optimized distorted structures reveals the presence of oxygen ions with BVS less than 2 (whereas some other

oxygen ion exhibits higher BVS to maintain charge balance). Oxygen with BVS less than 2 indicates these oxygen are underbonded and therefore more reactive toward reduction. This is directly observed in our H_2−TPR experiments. Transition-metal-ion- and noble-metal-ion-substituted ceria showed enhanced OSC compared to pure ceria (see Table 2). Negligible effect is observed for RE ion doped ceria; H_2−TPR for these materials shows little increment in OSC (see Figure S5 in the Supporting Information) compared to what has been observed for other dopant ions. This is clearly reflected in our DFT calculations. Simulated structure for RE doped ceria showed very little deviation from ideal bond length of 2.34 Å expected for pure ceria lattice. Thus the absence of substantial structural distortion makes the RE doped ceria very less susceptible to reduction in H_2.

Another important observation is the changes in OSC in presence of Pd ion for transition-metal-ion-substituted ceria. Our H_2-TPR experiment showed that in presence of dopant Pd ion, OSC of Fe-, Mn-, and Co-doped ceria showed tremendous increment in OSC at lower temperatures (see Figure 5a−c and also take note of Table 2). Therefore, dopant Pd ion stimulates some kind of synergistic effect due to which higher reducibility is observed at lower temperatures. Such high OSC in presence of Pd ion is not observed for Ni- and Cu-doped ceria (see Figure 5c, d). DFT calculations for these systems clearly reveal the reasons behind such observations from H_2−TPR experiments. Our simulations for Mn-, Fe-, and Co-doped ceria structure in presence of Pd dopant ions show further destabilization of lattice (see Figures 9−11; take note of *y*-scale). In addition to creating longer Pd−O bonds, one also observe clearly the presence of longer Ce−O, Mn/Fe/Co−O bonds. Bond valence analysis for these Pd- and Mn/Fe/Co-substituted ceria indicates that more oxide ions have BVS values less than 2 compared to the system without Pd ions (see Figure S6 in the Supporting Information). Therefore, with Pd-ion substitution, destabilization of the ceria lattice creates weaker oxide ions for Mn-, Fe-, and Co-substituted ceria systems. So the synergistic effect, namely enhanced reducibility at much lower temperatures for Mn/Fe/Co-doped cerium oxide, brought by Pd-ion substitution is directly correlated to the results obtained from our DFT calculations.

Similar results were not seen in the case of Ni- and Cu-ion-doped ceria structure. Our H_2−TPR experiments show very little gain in OSC and temperature with Pd ions substitution. Therefore synergistic effect brought by Pd ion substitution is less pronounced for the Ni- and Cu-doped ceria structure. Simulated optimized structure for Ni/Cu- and Pd-doped ceria (see Figures 11 and 12) show only longer dopant−oxygen bonds; longer Ce−O bonds are absent. The absence of longer Ce−O bonds in the presence of Pd ion points toward the lesser OSC expected of these materials. This in agreement with our experimental results, which showed little increase in OSC, unlike the Mn/Fe/Co-doped structure.

Acknowledgment. The authors thank Dr. Anil Kumar (JNCASR) and the central computing facility at JNCASR. U.V.W. acknowledges the funding from the DAE-SRC project grant. The authors gratefully acknowledge financial support from the Department of Science and Technology (DST), Government of India.

Supporting Information Available: Additional figures (PDF). This material is available free of charge via the Internet at http://pubs.acs.org.